

PIV Measurements in the Wake of a Full-Scale Rotor in Forward Flight

Alan J. Wadcock¹ and Gloria K. Yamauchi²
NASA Ames Research Center, Moffett Field, CA 94035

Eduardo Solis³
Monterey Technologies, Inc., Monterey, CA 93940

Ashley E. Pete⁴
University Affiliated Research Center, UC Santa Cruz, Moffett Field, CA 94035

Stereo Particle Image Velocimetry (PIV) measurements were acquired in the wake of a full-scale UH-60A rotor that was tested in the National Full-Scale Aerodynamics Complex 40-Foot by 80-Foot Wind Tunnel. Flow field velocities were acquired in a stationary cross-flow plane located at approximately 90 deg rotor azimuth. The region of interest was approximately 4-ft high and 13-ft wide and covered the outer half of the blade radius. All measurements were acquired in forward flight conditions. The laser and camera systems were synchronized with the rotor 1/rev so that measurements were acquired for different rotor blade azimuths. The design of the PIV system is described as well as the installation of the system components in the wind tunnel. Examples of measured velocity fields are presented. These measurements represent the first PIV measurements to be made in the U. S. on a full-scale rotor in forward flight.

Nomenclature

c	=	blade chord
CCW	=	counter clockwise
CW	=	clockwise
C_T	=	rotor thrust/ $(V_{tip}^2 \pi R^2 \rho)$
d_c	=	vortex core diameter
FOV	=	field of view
$FWHM$	=	Full Width Half Magnitude
LLS	=	laser light sheet
M_{tip}	=	blade tip Mach number, $V_{tip}/(\text{sound speed})$
PIV	=	particle image velocimetry
R	=	rotor radius
ROI	=	region of interest
V	=	free stream velocity
V_{tip}	=	rotor blade tip speed, ΩR
IPR	=	once per rev encoder signal
NPR	=	N per rev encoder signal
μ	=	advance ratio, $(\text{tunnel velocity})/V_{tip}$
ψ	=	blade azimuth measured CCW from fully aft location (plan view), deg

¹ Aerospace Engineer, Aeromechanics Branch, Mail Stop 243-12, Moffett Field, CA 94035

² Aerospace Engineer, Aeromechanics Branch, Mail Stop 243-12, Moffett Field, CA 94035

³ Industrial Design Engineer, 2400 Silver Cloud Court, Suite 103, Monterey, CA 93940

⁴ Mechanical Engineer, Mail Stop 19-26, Moffett Field, CA 94035

ψ_w	=	wake age; azimuthal position of generating blade measured CCW from LLS, deg
$\Delta\Psi$	=	azimuthal location of primary blade measured CCW from LLS, deg
σ	=	rotor solidity
Ω	=	rotor speed, rpm

I. Introduction

As the modeling fidelity of rotorcraft computational analyses improves, the need for validation data grows. For future experiments investigating aeromechanic and aero-acoustic phenomena, rotor airloads measurements are becoming a requirement in order to provide the minimum validation data for the CFD analyst. Grid refinement techniques¹ and adjoint methods² are providing improved resolution of the rotor wake, hence velocity measurements are now desired throughout the wake, not just near the blade tip. Coupled CFD and computational structural dynamics (CSD) analyses are now commonplace and require measurements of the elastic motion of the rotor blade for validation. Measuring *everything, everywhere, simultaneously* appears to be the challenge presented to the experimentalist.

A key activity within the Subsonic Rotary Wing (SRW) Project of the NASA Fundamental Aeronautics Program is the development and application of experimental techniques for rotorcraft (see Chapter 5 of Ref. 3). Recognizing the analysts' desire for measurements beyond rotor force and moment data, optical techniques are being incorporated into SRW-sponsored wind tunnel tests to provide flow field measurements⁴⁻⁶ as well as blade deformation⁷ and blade airloads data⁸. Applications of these techniques to rotary wing configurations can be extremely challenging, with the added complication of limited optical access in many facilities. In particular, optical techniques applied to full-scale rotors tested in the National Full-Scale Aerodynamics Complex (NFAC) 40-Ft by 80-Ft Wind Tunnel require many months of preparation prior to data acquisition. The blade deformation⁷ and retro-reflective background oriented Schlieren or RBOS⁶ techniques were implemented on a full-scale rotor for the first time during the UH-60 Individual Blade Control (IBC) test in the NFAC⁹. The IBC test served as a risk-reduction opportunity for these techniques and to a limited extent, for the stereo Particle Image Velocimetry (PIV) technique discussed in this paper. All three optical techniques were further developed after the IBC test in preparation for the UH-60A Airloads test¹⁰, completed in May 2010.

The UH-60 Airloads test¹⁰ was designed to acquire a suite of measurements to validate state-of-the-art modeling tools. Measurements included blade airloads, blade structural loads, rotor performance, blade deformation, and rotor wake measurements. In addition to parametric sweeps, test conditions simulated previously acquired flight test conditions and small-scale wind tunnel test conditions. Rotor stall and high-advance ratio conditions were also explored. This paper describes the design and installation of a stereo PIV system used to acquire rotor flow field velocities during the UH-60 Airloads test. The system design was largely driven by the constraints imposed by the 40-Foot by 80-Foot Wind Tunnel test section geometry and facility infrastructure. These constraints and other challenges are discussed, in addition to the selection of PIV test conditions. Finally, sample results are presented.

II. Description of the Facility and Test Article

The UH-60A Airloads rotor was tested in the National Full-Scale Aerodynamics Complex (NFAC) 40-Foot by 80-Foot Wind Tunnel at NASA Ames Research Center. The NFAC, which also includes the 80-Foot by 120-Foot Wind Tunnel, is managed and operated by the U. S. Air Force Arnold Engineering Development Center under a long-term lease agreement with NASA. The 40-Foot by 80-Foot Wind Tunnel has a closed circuit with an air exchanger. The closed test section is 80-ft long and 39-ft high, with semicircular sidewalls of 19.5-ft radius for an overall width of 79 feet. The maximum speed in the test section is 300 knots. The test section is treated with sound-absorbing material that enables aero-acoustic measurements.



Figure 1. UH-60A rotor installed on the Large Rotor Test Apparatus in the NFAC 40-Foot by 80-Foot Wind Tunnel.
American Institute of Aeronautics and Astronautics

The rotor was mounted in the test section on the Large Rotor Test Apparatus (LRTA). The LRTA is a multi-purpose rotor test stand with a rotor balance, fuselage load cells, two 3000-hp electric motors, and a rotor control system. The LRTA was mounted on a 3-strut support system in the test section. Varying the height of the tail strut enabled model angle-of-attack changes. Figure 1 shows the UH-60A rotor and LRTA installed in the test section.

Table 1. UH-60 Rotor Parameters¹²

Number of blades	4
Radius, ft	26.83
Nominal chord, in	20.9
Equivalent blade twist, deg	-18
Blade tip sweep, deg aft	20
Geometric solidity ratio	0.0826
Airfoil section designation	SC1095/ SC1095R8
Thickness, % chord	9.5
100% RPM	258

The UH-60A rotor is a 4-bladed articulated rotor that was flown during the UH-60A Airloads flight test program¹¹ in 1993-1994. Table 1 shows the key characteristics of the rotor. A plan view of the blade¹³ is shown in Figure 2. As in the flight test, one of the blades was instrumented with 242 pressure transducers. Figure 3¹⁴ shows the distribution of pressure transducers on the upper and lower surface of the airloads blade.

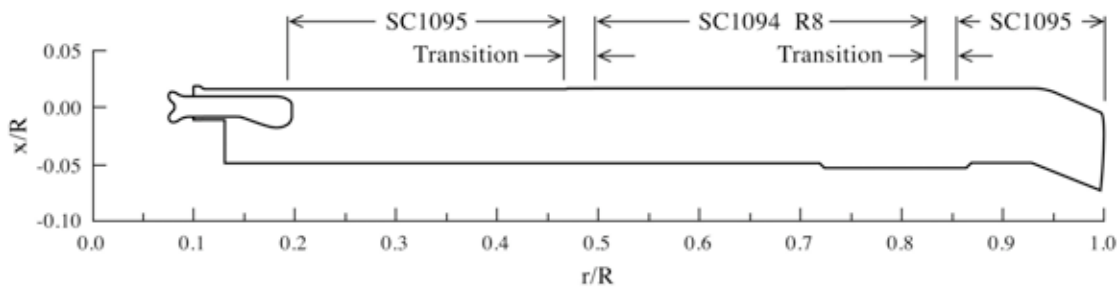


Figure 2. UH-60 blade planform¹³.

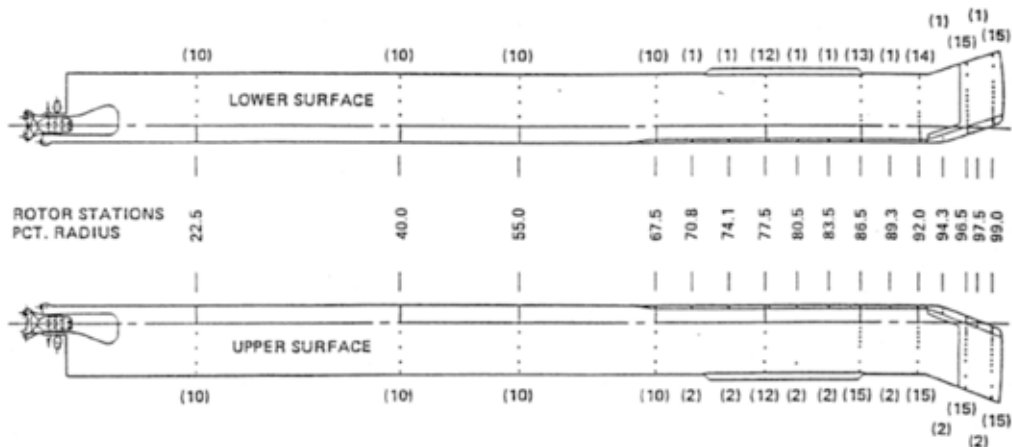


Figure 3. Pressure transducer distribution on UH-60A blade¹⁴.

III. PIV System Design

Figure 4 shows a sketch of the NFAC 40-Foot by 80-Foot Wind Tunnel test section. The ceiling and walls have a 4-ft thick acoustic lining with an outer steel shell, and the only optical access is via a limited number of facility camera ports. All the camera ports, shown in blue, are positioned in the first row of panels above the hinge line. Overhead clamshell doors located in the center of the test section rotate about the hinge-line on either side of the test section allowing models to be craned into and out of the test section.

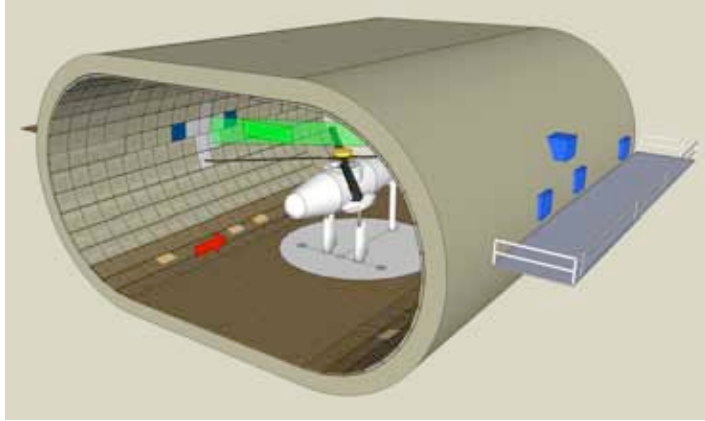


Figure 4. Acoustic lining of the NFAC 40-Foot by 80-Foot Wind Tunnel.

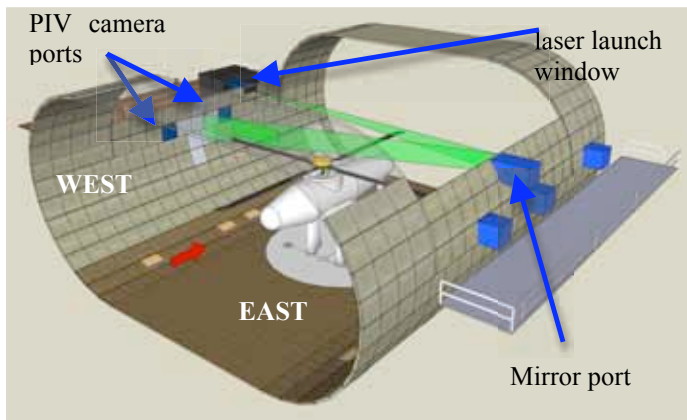


Figure 5. Laser launch window and NFAC facility camera ports.

covered with 1/4-inch aluminum plate and retro-reflective material for Retro-reflective Backward Oriented Schlieren (RBOS) rotor wake measurements⁶. The blue panels represent the existing facility camera ports. Note that the chosen LLS location is not equidistant between the two camera ports. For maximum overlap in the FOV between the two PIV cameras, the cameras were installed in each camera port at the most downstream positions possible, placing them about 8ft either side of the LLS.

At this point in the design the LLS position and the PIV camera locations are defined. The next step is to select a lens compatible with the desired FOV and required spatial resolution of the velocity measurements.

Previous experience¹⁵ has shown that 11 velocity vectors are adequate to describe the vortex core structure. Measurements by Leishman et al^{16, 17} on 1- and 2-bladed model-scale rotors operating *in hover* at reduced tip speed

PIV data were acquired in the vicinity of the blade tip on the advancing side of the rotor disk, in the cross-flow plane, as close to azimuth 90 degrees as possible. The advancing side of the rotor disk is technically of more scientific interest. Also, by placing the laser light sheet (LLS) close to $\psi = 90^\circ$ there would be less difficulty in understanding the generated wake by following the wake evolution as each successive blade passed through the sheet. The most difficult decisions were how to project the LLS into the test section and steer it to the area of interest and where to mount the cameras. The simplest (least expensive) approach was to utilize the existing laser launch window to project the laser into the test section and, using a large format mirror mounted inside the opposite sidewall (at the stream wise station of interest), to re-direct the LLS in the cross flow plane towards the advancing blade tip.

Figure 5 shows the existing laser launch window in the West wall of the test section. A new mirror port is shown in the East wall. With the mirror port as drawn, the LLS can pass downstream of the instrumentation hat (MUX bucket) atop the rotor shaft and still reach the area of interest. Figure 5 shows the selected LLS position in the Trefftz plane, as far downstream from the MUX bucket as possible to permit at least a minimum amount of nose-up rotor operation before the MUX bucket enters the LLS and impacts the available PIV ROI. The white wall panels represent acoustic wall panels that have been

indicate a minimum core size defined by $d_c / c = 0.10$ at early wake age. The nominal chord for the UH-60A rotor is 20.9 inches so this indicates a minimum core diameter d_c of 2.09 inches. The goal is to have 11 velocity vectors inside the core so this defines the distance between vectors as 0.209 inches. Experience has shown that a cross-correlation window size of 24 x 24 pixels is achievable without too much difficulty. Assuming the data are processed using 50% overlap the vector spacing becomes 12 pixels in both X and Y.

The cameras selected for these measurements were TSI PowerView Plus 11Mp cameras having 4008 x 2672 pixel resolution, square pixels of size 9.0 μ m and 12-bit dynamic range. The sensor size is 36.07 mm (H) x 24.05 mm (V). A protective mask reduces the effective sensor size. From above, in the vertical direction 12 pixels need to correspond to 0.209 inches in order to achieve the desired spatial resolution in the velocity measurements. Using the manufacturers pixel size information, the vertical magnification, M, becomes 0.02034. From thin lens theory, the lens focal length is given by

$$f = M u / (1 + M)$$

Substituting $M = 0.02034$ and using the approximate horizontal distance from the lens to the center of the FOV of 21 ft (object distance, u) we obtain $f = 128$ mm. Using $M = 0.02034$ and the sensor height of 24.05 mm yields a flow field FOV height of $24.05 / 0.02034 = 1182$ mm or 46.6 inches. The PIV ROI is approximately 4ft high. Using the approximate 8-ft camera off-axis location, the radial extent of the PIV ROI is estimated to be 14.6ft.

In the vertical direction we have that 2672 pixels = 1182 mm, or 1 pixel (V) = 0.44 mm = 0.017 inches. In the radial direction, however, we have 14.6 ft = 4008 pixels, or 1 pixel (H) = 1.11 mm = 0.044 inches. If a cross-correlation window of size 24 pixels is used with 50% overlap, vector spacing becomes 12 x 0.017 = 0.204 inches (V) and 12 x 0.044 inches = 0.53 inches (H). This yields 11 vectors inside the core in the vertical direction but only 5 vectors inside the (minimum expected) vortex core in the radial direction. This is unacceptable. If processing is performed with 75% overlap, the smallest expected vortex can be expected to yield 21 vectors across the core in the vertical direction and 9 vectors across the core in the radial direction. This is acceptable for the definition of the internal vortex structure.

The closest readily available lens focal length that matches the calculations is 120 mm. For small sensors, Nikon 35mm format lenses are acceptable. Nikon 35mm format lenses have a circle of illumination appropriate for 35mm film, namely 36 mm x 24 mm. Note that this is almost identical to the physical size of the current sensor. Medium format lenses have a larger circle of illumination appropriate to 120-format typical of roll film (6 cm tall). For this reason, a pair of medium format SMC Pentax-FA 645 Macro 120mm F4.0 lenses was selected for the current study. SMC stands for Super Multi Coat, which is a Pentax lens coating designed to greatly reduce unwanted reflections inside the lens, and 645 refers to the film size, nominally 6 cm x 4.5 cm (actual image size 56 mm x 42 mm). The larger circle of illumination provided by the medium format lens allows the PIV ROI to be adjusted +/- 18 inches vertically without vignetting of the image. This provides the desired flexibility in the camera mount to adjust the vertical location of the PIV ROI by +/- 1.5 ft about the nominal design position without having to re-design the installation.

The optimal vertical location for the PIV ROI was determined computationally. CAMRAD II calculations were performed for a series of rotor test conditions representative of expected PIV measurements and the tip vortex trajectory and trailed vortex sheet examined for where they intersect the plane of the LLS. Figure 6 shows a typical frame, from a movie created from a CAMRAD II computation for a PIV test condition of interest. This image is included to illustrate the complexity present in a typical rotor wake. One blade shows the blade loading distribution in the radial direction at a particular blade azimuth position. By playing the movie, the blade loading distribution can be examined at any azimuth of interest. The wake shed from each blade is color-coded to differentiate between individual blades. Blade position and shape represent both rigid body displacements at the hub plus aero-elastic deformation. The PIV ROI is drawn at azimuth 90 degrees, covering the outer 50% of the blade radius. Where any trailed vortex filament cuts the PIV ROI a marker is placed to identify the vortex trajectory as a function of blade position relative to the laser sheet. This particular test condition shows vortex sheet roll-up at the blade tip and also roll-up of the inboard sheet into an inboard trailed vortex. By examining a range of expected PIV test conditions computationally in this manner, the PIV ROI was finally chosen such that the mid-height of the ROI was 22.41 ft above the test section floor (2.0 ft above the rotor hub) with outermost edge approximately 1 ft beyond the rotor tip. Expected size of PIV ROI was 4 ft (V) x 14 ft (H).

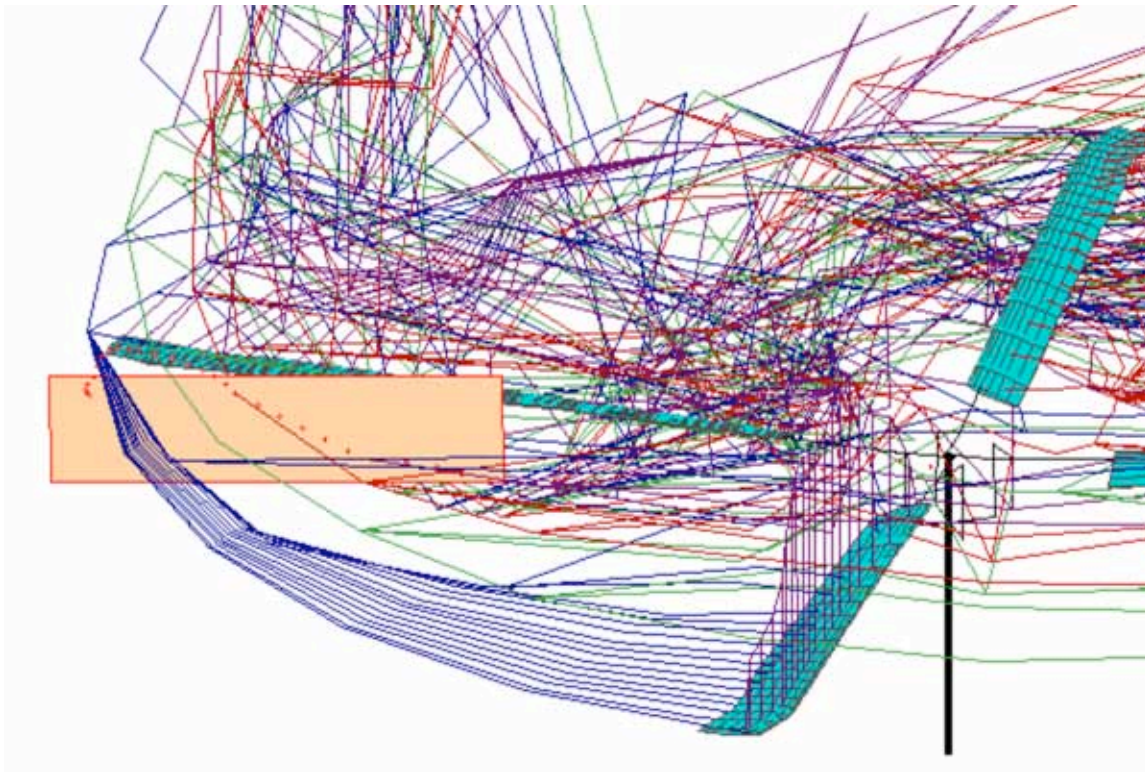


Figure 6. Single frame from CAMRAD II movie.

The LLS thickness was chosen to be 3/16 inch. The laser pulse interval was chosen to limit the particle displacement normal to the LLS to one-sixth the sheet thickness, improving the correlation strength (compared to using $\frac{1}{4}$ the sheet thickness) but compromising the accuracy of individual displacement measurements. This leads to an apparent uniform in-plane horizontal particle displacement of -2 pixels due to the out-of-plane velocity component (the free stream). Estimating the peak tangential velocity associated with the rotor tip vortex to be $0.3\Omega R^{16,17}$ leads to a maximum estimated in-plane particle displacement from the tangential velocity associated with the tip vortex of ± 2 pixels. Thus the expected particle displacements measured by each camera are in the range $-4 < \Delta x < 0$, $-2 < \Delta y < 2$ indicating a maximum particle displacement of 4 pixels. If the random uncertainty in the measurement of any individual isolated particle displacement is estimated to be 0.1 pixels, the expected uncertainty in the instantaneous displacement field of each camera is estimated to be 2.5% of the maximum displacement measured in the field. By acquiring a population of 100 instantaneous PIV vector fields, the estimated uncertainty in the mean velocity field can be reduced to 0.3% of the maximum velocity in the field.

III.A. Cameras

Each PIV camera was mounted inside an NFAC facility camera port. All the facility camera ports are located in the first row of wall panels immediately *above* the hinge line of the overhead clamshell doors. Thus, opening the test section overhead doors was minimized to prevent movement of the camera-lens assemblies and invalidation of the camera calibrations.

The standard facility camera port contains a rollout frame, or carriage, for ease of access to equipment installed inside the port. To provide a rigid base on which to mount the PIV cameras, 0.5-inch thick aluminum plate was installed on the top of each carriage to provide flexibility in locating each camera inside the port. Each carriage was then clamped to the underlying rails on each side of the camera port to prevent movement caused by tunnel vibration during a run, and also preventing gross motion of the carriage if the overhead clamshell doors were opened.

A pair of TSI PowerView Plus 11Mp cameras with 4008 x 2672 pixel resolution and 12-bit dynamic range was used for the current measurements. Square pixels of size 9.0 μm result in a sensor size of 36.07 mm (H) x 24.05 mm (V). Maximum listed PIV frame rate is 2.4 frames/sec. Both PIV cameras were operated in forward scatter mounted

an approximately equal distance either side of the LLS in order to maximize the overlap of the two camera fields of view (Figure 5). Sophisticated (i.e., complex) camera mounts were designed with the IDT proVision “simple” calibration in mind.



Figure 7. Downwind PIV camera.

camera pitch, roll and yaw. A third spacer follows immediately ahead of the sensor to block IR illumination from the NFAC IR facility camera used to illuminate the model during periods of “lights out” testing required by PIV data acquisition. This filter passes visible light in the wavelength range 400 to 700 nm whilst filtering out all UV radiation and blocking long wavelength radiation in the near infrared and above.

At the base of the stack supporting the lens is a micrometer-driven linear translation stage providing adjustment to the FOV in the vertical direction. Once this translation stage was in the desired position, shims were placed underneath the drive to support the assembly at the desired height and the unit was locked out. This translation stage drives a horizontal platform that supports a second micrometer-driven linear translation stage that provides motion along the axis of the lens, for conventional focusing. A medium format SMC Pentax-FA 645 Macro 120mm F4.0 lens is mounted at the top of the stack. In front of the lens is a remotely operated large aperture electronic shutter.

An analog video camera is shown in Figure 7 mounted adjacent to the downwind PIV camera. This analog camera was used to provide continuous real time video covering an area somewhat larger than the PIV ROI. The analog video was particularly useful when determining the local PIV origin for each test condition. With the shutters closed in front of each PIV lens, the blade position relative to the LLS at the instant the lasers fired was adjusted (using the delayed IPR trigger signal) until the trailing edge of the reference blade was barely touching the laser sheet. To avoid damaging the PIV cameras during this maneuver the PIV cameras were shuttered and the procedure observed using the analog video camera.

Figure 7 shows the downwind PIV camera installation. Figure 8 shows a close-up view of the upwind camera assembly. At the base of the assembly there is an interface plate that ties the assembly to the 0.5-inch thick carriage platform. A turntable, consisting of two circular plates separated by a series of vibration isolation dampers, provides coarse adjustment of the camera FOV and is lockable at three points on its perimeter. For the current study, three solid aluminum blocks were inserted between the top and bottom plates of the turntable to lock out these dampers and achieve a rigid mount. The turntable supports a square breadboard on which the camera-lens assembly is mounted. At the base of the stack supporting the camera there is a spacer followed by a micrometer-driven linear translation stage providing adjustment in the radial FOV. Then follows a second spacer with a micrometer-driven rotary stage for Schiempflug focusing. This is followed by a tilt stage providing micrometer-driven adjustment in



Figure 8. Upwind PIV camera.

IIIB. Critical Camera Focusing

Camera focusing was carried out using a pair of plumb-bob rods, nominally 1/8-inch diameter, carefully positioned in the center of the 3/16-inch thick LLS using remotely controlled actuators. The Nd:Yag laser was then turned off and the plumb bob rods illuminated using white light. A green Kodak Wratten filter No. 99 was placed in front of each camera lens to minimize any chromatic aberration and the shutters opened. After each camera was focused, all micrometers were locked in place using aluminum tape. The same filters were used during the acquisition of camera calibration images and then removed.

IIIC. Laser, Optics & Laser Timing

Figure 9 shows the outside view of the Laser Safety Enclosure (LSE) at the 4th floor. This is a custom-made enclosure fabricated from 80/20 aluminum extrusions and laser safety curtain. To allow the clamshell doors to remain functional, the enclosure is in two parts. The inner walls telescope freely inside the outer walls. In this manner, the inner walls of the LSE can be retracted resulting in minimal impact on the test section overhead door operational envelope. Refer to later section for discussion of laser safety interlocks and safety protocols.



Figure 9. Laser Safety Enclosure.

A Spectra Physics PIV-400 Series pulsed Nd:Yag laser was used for the current series of PIV measurements. This is a dual head laser capable of delivering 350mJ/pulse at 532nm for a laser rep rate of 15Hz. Pulse width is 5 – 8ns, beam diameter is 9mm and beam divergence is less than 0.5mrad (full angle measured at FWHM points). The laser was re-tuned for the current investigation to operate at the rotor 1PR frequency of 258 RPM or 4.3Hz.

Figure 10 is a view of the optical table inside the LSE. Immediately to the left of the laser head is a black-anodized plate that acts as a beam block during laser warm up. In the background is a remotely operated beam dump. Also shown is a Laser Power Meter sensor head and display. After laser warm-up is complete, laser power is measured separately for each beam. The output beam from the laser head passes through a high-energy 2X beam expander to aid in long-range focusing of the LLS. A high-energy mirror then directs the laser beam vertically upwards along a periscope structure mounted atop the optical table. At the top of the periscope, a second high-energy mirror re-directs the laser beam horizontally into the Laser Launch Port. The Laser Launch Port contains a series of high-energy beam steering mirrors and a pair of cylindrical lenses (+100mm and -100mm) mounted on a goniometer in order to rotate the LLS entering the test section into the desired vertical plane. The cylindrical lens pair was adjusted to obtain the desired LLS spreading angle in the vertical direction.

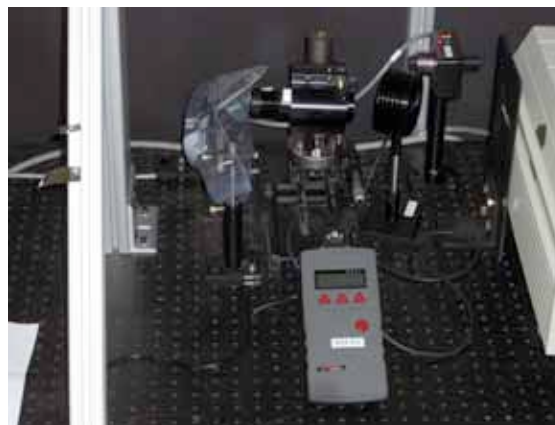


Figure 10. Optical table inside the LSE.

The LLS was deliberately over-expanded in the vertical direction to a height of about 5 ft at the large format mirror. The large format mirror is 3-ft tall, implying that the top and bottom 12 inches of the LLS miss the mirror and are not reflected cross-stream to the PIV ROI. The top and bottom of the LLS are necessarily thinner than the middle of the sheet and are therefore unusable. Approximately 75% of the laser pulse energy is reflected cross-stream to the PIV ROI and the LLS has a more uniform thickness from top to bottom.

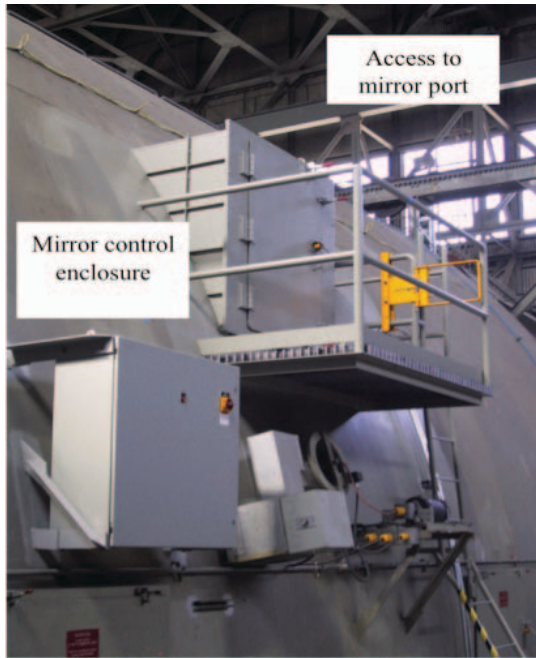


Figure 11. Mirror Port completed.

accounts for the high-resolution 4,096,000 pulses/rev encoder on the yaw controller and the low-resolution 655,360 pulses/rev encoder on the pitch controller. One degree of rotation in yaw of the mirror produces two degrees of rotation in yaw of the LLS. The minimum motor step size was set to 4 encoder pulses resulting in a minimum stream wise LLS motion of 0.012 inches on the far wall of the test section.

Figure 12 is a sketch of the large-format mirror installation showing a 6-in wide x 36-in tall mirror installed in the mirror port. This was eventually replaced with a 12-in wide mirror to provide greater freedom in placing the mirror inside the mirror port.

Laser light sheet

The desired stream wise location of the LLS was identified by a pair of reference lines on the West wall of the test section close to $\psi = 90$ degrees as shown in Figure 13. Two 8-ft tall pieces of adhesive-backed 1-in wide soft aluminum tape placed 1/4-inch apart were applied to the RBOS sidewall panels and then painted matte black. The space between these strips of black tape is only slightly wider than the thickness of the LLS. Any small stream wise motion of the LLS takes the LLS off the retro-reflective material of the RBOS panel and onto the black tape and this is easily monitored using a facility camera. Fluorescent lights immediately surrounding the facility camera helped compensate for the extreme intensity of the LLS and provided improved contrast of the alignment marks.

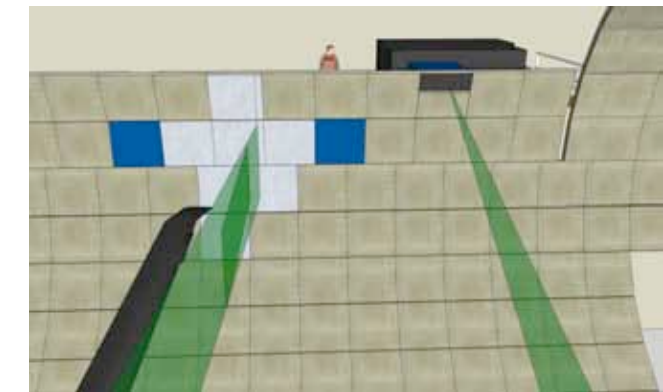


Figure 13. LLS reference lines on West wall.



Figure 14. Beam tailoring optics on zigzag beam inside laser head.

The design LLS thickness was chosen to be 3/16 inches (see section III). The center of the PIV ROI is in excess of 160 ft from the laser head (60 ft from the large format mirror). Not only did this make beam steering very sensitive but also necessitated considerable effort in matching the LLS thickness of the two laser beams. The two laser beams do not have identical beam divergence properties, and at long range this results in considerable differences in LLS thickness. Beam tailoring optics (a matched spherical plano-convex and plano-concave lens pair) were therefore installed in the optical path of the zigzag beam inside the laser head as shown in Figure 14. The separation distance between the two lenses could then be adjusted to control the beam divergence of the zigzag beam and match the long-range beam diameter to that of the straight beam.

LLS thickness measurements were repeated separately for each beam. Careful measurements of LLS thickness over the whole of the PIV ROI indicated a sheet thickness of 7/32" +/- 1/32". The LLS could not be focused any tighter than this, and the LLS thickness was essentially constant over the full length of the ROI.

III.D. Laser timing and synchronization

The Spectra Physics PIV-400 Series pulsed Nd:Yag laser (rated at 400mJ at 532nm at 15Hz rep rate) was re-tuned for the current investigation to operate at the rotor 1PR frequency of 258 RPM or 4.3Hz.

The 1PR trigger pulse is generated by the primary blade (pressure-instrumented blade) passing aft of the rotor hub. The sequence of blade passage past a fixed point in space is primary (red), followed by black, then yellow (strain-gauged blade) and finally blue. The maximum number of encoder NPR steps/rev available at the Rotor Control Console (RCC) was 4096/rev. This was used as input to the custom-made Delayed 1PR Trigger Box.

The TSI PowerView Plus 11 Mp PIV cameras are rated for 4.3Hz frame rate (2.15 PIV frame rate). If a trigger is input to the camera and the camera is not ready, it will wait until the following trigger pulse arrives. The rotor 1PR frequency is 4.3Hz so this is too fast for the PIV cameras in straddle mode, but every second 1PR at 2.15Hz should work fine. Static testing using a simulated rotary shaft encoder trigger revealed significant frame dropout caused by the camera not being ready to acquire data from consecutive pulses at 2.15Hz. Chosen operation was therefore to use the laser rep rate that avoided dropped frames, namely 0.61Hz. Decimation of the 1PR to achieve the desired 0.61Hz trigger rate was performed in Software (TSI Insight 3G). One hundred PIV frames acquired at 0.61Hz required 164 seconds.

The desired Q-switch Δt is selected using Insight 3G software. The expected range for Δt for the current study was 10 to 20 μsec . For such a relatively short laser pulse interval, measurement of the corresponding *laser emission* pulse interval was necessary, as the difference can be significant between the two time intervals. A digital scope was used to verify the timing of the flash lamp and Q-switch trigger signals delivered by the TSI synchronizer. A photodiode, mounted behind the high-energy mirror at the base of the periscope on the optical table, was used to determine the delay between the Q-switch trigger and laser emission for each laser rod, with the result that

$$\Delta t_{\text{emission}} = \Delta t_{\text{Q-switch}} + 110 \text{ nsec} \quad (+/- 2 \text{ nsec for } 5 < \Delta t_{\text{Q-switch}} < 40 \mu\text{sec})$$

Velocity measurements need to be adjusted for this additional 110 nsec delay between laser emissions compared to the software input Q-switch delay.

Synchronizer Box Bypass

A TSI LaserPulse Synchronizer Model 610035 was used to automate control of the timing between laser pulses and PIV cameras. The Synchronizer, via TSI Insight 3G Software, controls all timing necessary to collect frame-straddled images. Signals for the laser flash lamps and Q-switches, the camera, and the frame grabber are generated and automatically synchronized. An external trigger option allows for phase-locked velocity measurements.

The camera controls the Synchronizer. If the camera is not ready when the external trigger is received, flash lamp and Q-switch triggers are inhibited, and the camera waits for the next trigger. If the input trigger is faster than 0.61Hz the camera will drop frames and the flash lamps will trigger at sporadic intervals.

In order to drive the flash lamps at the 4.3Hz rep rate the laser was tuned for, independent flash lamp triggers were generated for each 1PR external trigger using a Digital Delay Generator model DG535. Timing of these pulses was measured using a digital scope to verify agreement with the Synchronizer outputs. Using these independent flash lamp triggers, the flash lamps were continuously driven at the 1PR frequency of 4.3Hz thereby keeping the laser rods hot and maximizing the laser emission, whereas the Q-switch trigger pulses drove laser emission at the reduced frequency of 0.61Hz (the PIV frame rate).

At the reduced laser rep rate of 0.61Hz, laser power at 532nm was measured to be 0.165Watts (270mJ/pulse) for the straight beam and 0.175Watts (285mJ/pulse) for the zigzag beam.

III.E. Smoke Generators

In the current test, four MDG MAX 5000 HO (High Output) seeders were installed *on the floor* of the settling chamber, upstream from the test section. The seeders were uniformly distributed across the settling chamber with lateral spacing equal to 20% of the settling chamber width as shown in Figure 15. The smoke generators use MDG NEUTRAL, a mineral oil based fog fluid. Nitrogen is used as a propellant when generating fog, and for purging the heating modules when the automatic purge cycle is initiated. The nitrogen cylinders were located outside the tunnel circuit, a separate cylinder for each smoke generator in order to maximize available run time. Nitrogen pressure of 35psi was chosen for the current test.



Figure 15. Seeder installation in settling chamber.

Smoke passes downstream along the floor of the settling chamber, into the contraction cone, and so into the test section. When all seeders were operating, four discrete smoke tubes several feet in diameter could be seen flowing down the length of the test section just above the floor into the primary diffuser. The adverse pressure gradient of the diffuser transfers energy from the mean flow into turbulence and helps diffuse the smoke tubes. After one complete circuit of the wind tunnel, the smoke arrives back in the test section uniformly distributed as desired.

Each MDG MAX 5000 HO smoke generator produces particles of size 0.5 to 0.7 micron diameter. The seeders were controlled remotely from the PIV station. An NFAC facility IR camera was deployed in the settling chamber to remotely monitor the status of each of the seeders, to ensure that each seeder remained operational and turned on and off on command, as desired, with the video monitor positioned at the PIV station. Figure 16 shows all 4 seeders operating in the settling chamber.



Figure 16. All 4 seeders shown operating in the settling chamber.

One important consequence of smoke injected at the floor of the settling chamber is that it takes a significant time before the injected smoke appears at the PIV ROI in the test section. The time of flight around the 40-Foot x 80-Foot wind tunnel circuit is given by the following equation

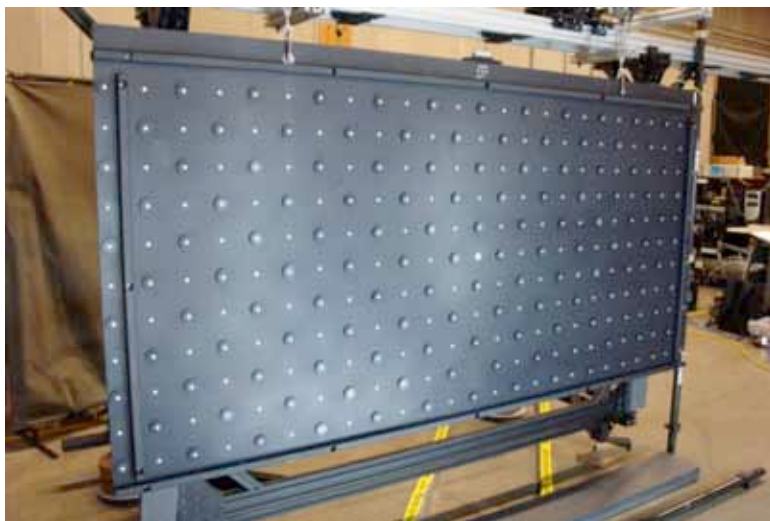
$$\text{Time of Flight, seconds} = 8703.7 / V \text{ (ft/sec)}.$$

where V is the test section velocity. Hence for a typical test section velocity of V = 150 knots = 253.33 ft/sec, Time of Flight = 34.4 seconds. This implies a lag of about 30 seconds between turning the seeders on and seeing a noticeable increase in seed density in the PIV ROI. Once the desired seed density is achieved (observed) in the test section, the seed density will continue to increase for the next 30 seconds.

Three Air Exchange (AE) settings are available --- 0%, 50% and 100% AE. These settings correspond to air exchange closed, or air exchange open with area ratio either 5% or 10% of the local duct area. PIV data runs were executed with the intermediate air exchange setting of 50% AE. Seed uniformity was not a problem. Maintaining the desired seed density in the PIV ROI was challenging however. Fresh seed was necessary for each PIV data acquisition. This was both time-consuming and inefficient.

IIIF. Camera Calibration

Camera calibration using the TSI software requires either a dual-plane calibration plate or a traversing single-plane plate. The size of the ROI and the ROI location in the test section quickly drove the plate design to a dual-plane plate. Fabricating a dual-plane plate to match the dimensions of the ROI (roughly 4-ft high by 14-ft wide) would make handling the plate cumbersome. In addition, the plate would be difficult to keep stationary while hanging over 20 ft in the air, and making a plate (composite or metal) that is flat over 14 ft would be prohibitively



a) Dual-plane calibration plate (targets are mirrored on opposite side of plate). **b) Close-up of flush and raised targets.**

Figure 17. Dual-plane calibration plate.

expensive. As a compromise, a 4-ft high by 8-ft wide dual-plane plate was designed and constructed (see Fig. 17(a)). The plate support system allowed the plate to be positioned so as to cover either the inner or the outer region of the ROI, requiring a camera calibration for each position of the plate. The two positions had a 2-ft wide overlap in the center of the ROI.

The plate is 96.5-in wide, 48.5-in high, and 0.25-in thick and made of MIC 6 aluminum. MIC 6 was selected over other metals for its cast granular structure and stress-relieving properties, enabling an acceptable flatness tolerance of the finished plate. Using a water jet, an 11 x 25 array of 0.375-in diameter holes was drilled into the plate. A fiducial mark was drilled at the plate center. A flat black sulfuric anodize Type II finish was then applied to the plate. To create targets flush with the plate surface, 0.25-in long pieces (targets) were cut from a 0.375-in diameter 7075 aluminum rod. Each target face was sandblasted to provide a satin finish. The target was then press-fit into the 0.375-in hole in the plate with Loctite applied to secure the target. The result was a 0.375-in diameter diffuse-reflecting target, flush on both sides of the plate. To create a dual-plane plate (i.e., each side of the plate has two planes), raised targets were fabricated and installed at every other hole location on the plate. Each raised target was embedded in a 1.5-in diameter washer that was cut from 0.25-in thick MIC 6 aluminum plate using a water jet. A 0.375-in hole was drilled at the center of each washer. The washers were anodized using the same finish as the plate. Similar to the flush targets, targets were press fit into each washer. Each washer was tapped at the bottom so that pairs of washers positioned on opposite sides of the plate could be secured together through a hole in the plate with a setscrew. Figure 17(b) shows a flush and raised target. The finished plate, shown in Fig. 17(a), consists of 137 flush targets (including the fiducial mark) and 138 raised targets on each side of the plate. The design distance between adjacent target centers is 10 cm or 3.937 inches. To minimize warping of the plate, square steel tubing was installed on all 4 edges of the plate, on both sides of the plate (Fig. 17(a)). The total weight of the plate was approximately 190 lbs.

Though the test section is 79-ft wide at mid-height, the usable floor of the test section is only 40-ft wide. Since the UH-60A rotor radius is 26.83 ft, nearly 7 ft of the rotor blade overhangs the curved sides of the tunnel walls at the ROI location, further complicating the design of the calibration plate support. Positioning the plate to cover the outboard section of the ROI required counterweights on the air stand. From start to finish, the camera calibration for the inboard and outboard positions of the plate required 3 days. Figure 18 shows a graphic of the calibration plate in the test section.

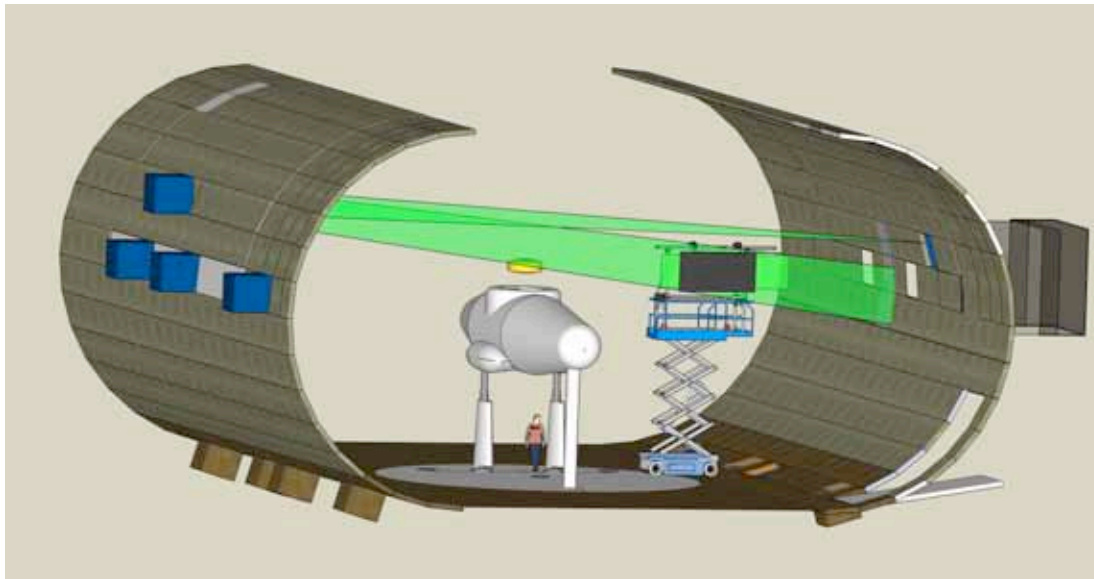


Figure 18. Overall view of the dual-plane calibration plate installed in the test section.

The support system required an air stand outfitted with a complex arrangement of custom components. The main members of the support framework were made from lengths of 80/20 (Figure 19). By far the most challenging aspect of the calibration procedure was placing the calibration plate in the LLS at the desired ROI. The support was designed so that the plate hung from two linear bearing systems and could be translated stream-wise into the cross-flow plane using micrometer drives. Rather than maneuver the plate directly into the sheet, the two rods used for camera focusing were attached to linear bearing systems (one rod for each linear bearing system) a fixed distance downstream of the plate. Figure 19 shows the plate and rods. The distance between the rods and the plate (1.25 in) remained fixed by using shims. The rods are much easier to position in the laser sheet compared to the plate, which was difficult to keep stationary. Once the rods were positioned in the sheet, the shims were removed and the plate translated to the location of the rods. The laser sheet was verified to intersect the middle of the vertical

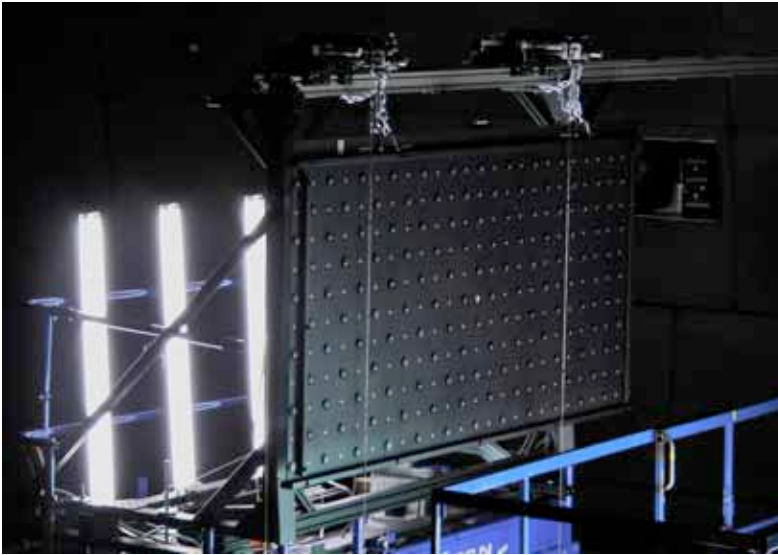


Figure 19. Calibration plate with positioning rods.

edge of the plate. The laser was then turned off, both sides of the plate were illuminated, and calibration images were acquired. White light was used for the calibration images, but green Wratten filters were mounted ahead of each camera lens to approximate the wavelength of the Nd:Yag laser and minimize any chromatic aberrations present in the lenses. Immediately after the calibration images had been acquired, these Wratten filters were removed. Figures 20(a) and 20(b) show the plate positioned in the inboard and outboard locations, respectively.

edge of the plate. The laser was then turned off, both sides of the plate were illuminated, and calibration images were acquired. White light was used for the calibration images, but green Wratten filters were mounted ahead of each camera lens to approximate the wavelength of the Nd:Yag laser and minimize any chromatic aberrations present in the lenses. Immediately after the calibration images had been acquired, these Wratten filters were removed. Figures 20(a) and 20(b) show the plate positioned in the inboard and outboard locations, respectively.



a) Inboard plate position



b) Outboard plate position

Figure 20. Calibration plate in position for camera calibration.

Figure 21 shows the calibration image (inboard plate position) acquired by the downstream PIV camera. Note that the rods and lights create hot spots in the image. Using Adobe Photoshop CS4, extraneous features of the image that interfere with the calibration software were masked. Figure 22 is the result of applying a mask to Figure 21.



Figure 21. Unmasked calibration plate image acquired by downstream PIV camera.

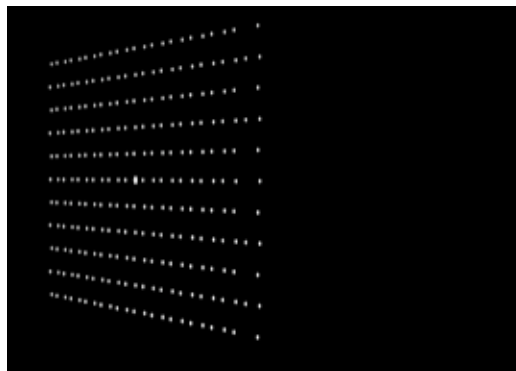


Figure 22. Masked calibration plate image acquired by downstream PIV camera.

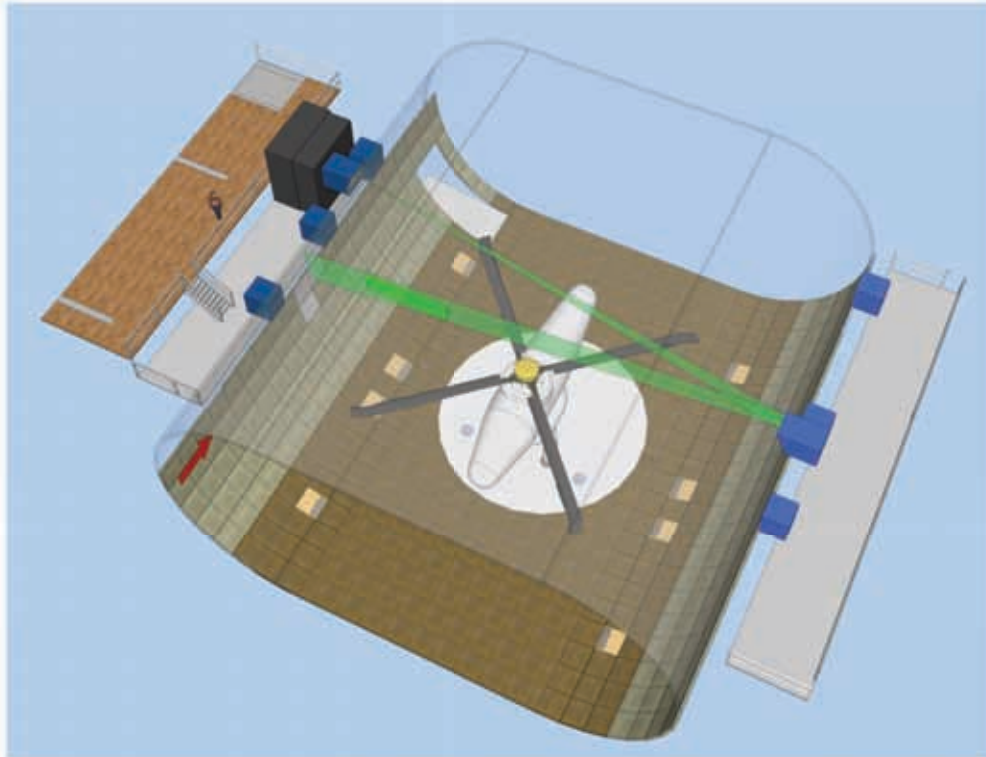
III.G. Safety Controls

The Laser Operator operates the laser system remotely from the PIV station inside the Computer Room on the 2nd floor whereas the Personnel Access Door to the test section is on the 3rd floor and the Laser Safety Enclosure is on the 4th floor. Lack of direct visual control over the hazard area complicates laser safety in such a large industrial wind tunnel as the NFAC, where both the laser and the test section are both remote from the operator. Integrating Class IV laser operations with full-scale rotor testing requires well-choreographed procedures and test crew vigilance at all times. Figure 23 is a cut-away of the wind tunnel and test section showing the location of the PIV cameras, laser enclosure, large-format mirror, and the PIV data acquisition system.

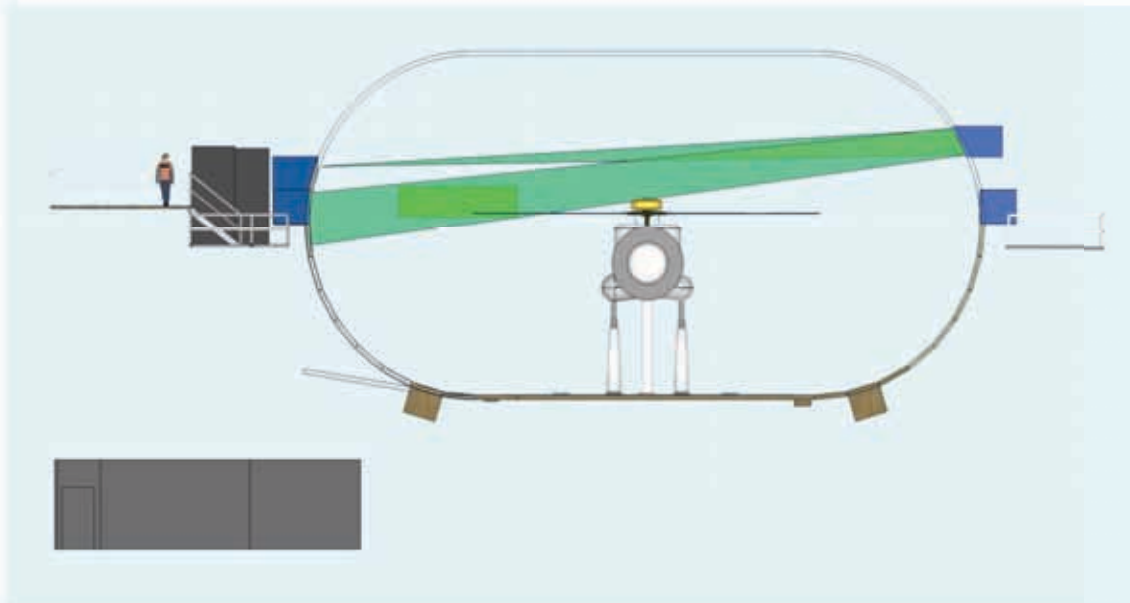
The laser enclosure on the 4th floor consisted of 80/20 framework covered with laser safety curtains. An interlock system was installed across the walkway leading to the laser enclosure. If the interlock was interrupted, the power to the Q-Switch would be cut, but the flash lamps would continue firing. Another interlock was installed across the entry to the test section. The power to the Q-Switch could be reset remotely if either interlock was interrupted. Emergency laser power “dump” units were placed inside the laser enclosure (4th floor), outside the laser enclosure (4th floor), outside the test section entry (3rd floor), and at the PIV data acquisition station (2nd floor). If the power to the laser power supply were dumped in an emergency, the power would have to be reset manually. A lockout, tag-out key system controlled access to the test section, all camera ports, all test section observer stations, the laser launch window and the port with the large-format mirror. In short, any window or door that gave a person visibility into the test section was controlled. In addition, warning signs posted around the facility and flashing red lights provided additional alerts to test personnel when laser operations were in progress.

IV. Test Procedures

The UH-60A Airloads rotor system and LRTA subsystems were warmed up prior to a forward flight run by operating the rotor in hover for approximately 45 minutes. During the warm-up, the laser was released into the test section. The laser sheet position was adjusted in the stream wise direction using the remote-controlled large format mirror. Alignment marks placed on the east wall of the test section were used to guide the laser sheet into position. After completion of the hover warm-up, rotor RPM was reduced to zero and reference data points for the rotor and model instrumentation were acquired. Rotor RPM was then increased to full tip-speed, the wind tunnel drive system was started, and velocity in the test section began to increase toward the target value. Seed was released from all 4 MDG seeders as tunnel velocity increased. Controlling the amount of seed was an iterative and time-consuming process. Though all 4 seeders were used at the start of a run, only one or two seeders were used between PIV data points to avoid saturating the flow field with seed. The wind tunnel air exchange was set at 5% for all PIV data runs to help prevent overheating the test section and to aid in removing excess seed.



a) Overhead view of PIV installation



b) View looking downstream

Figure 23. PIV system installation in the 40-Foot x 80-Foot Wind Tunnel test section.

The UH-60A rotor rotates in the counter-clockwise direction when viewed from above. Blade azimuths (ψ) of 0 deg and 180 deg correspond to the blade over the tail and the nose of the LRTA, respectively. The LLS was located at approximately $\psi = 90$ deg, as shown in the two views of Fig. 23. With the rotor shaft vertical, the LLS was located 21.50 inches downstream from the rotor hub location, as indicated in Figure 24.

Desired test conditions were typically defined by a combination of non-dimensional rotor thrust (C_T), advance ratio (μ), hub moments, shaft angle, and blade tip Mach number (M_{tip}). Once the specified conditions were achieved, the primary (pressure) blade was positioned such that the blade tip trailing edge intersected the laser sheet in the PIV ROI. This corresponds to the condition $\Delta\Psi = 0$ deg as shown in Fig. 24.

The primary (pressure-instrumented) blade is defined as Blade 1. The remaining blades are consecutively numbered as they pass over the tail of the LRTA as shown in Fig. 24. The delayed azimuth, $\Delta\Psi$, refers to the position of Blade 1 relative to the LLS. For example, $\Delta\Psi = 30$ deg corresponds to Blade 1 being 30 degrees ahead of the LLS as illustrated in Fig. 24. Note that this defines blade position in terms of *shaft rotation* relative to the reference position and neglects changes in lead-lag blade motion.

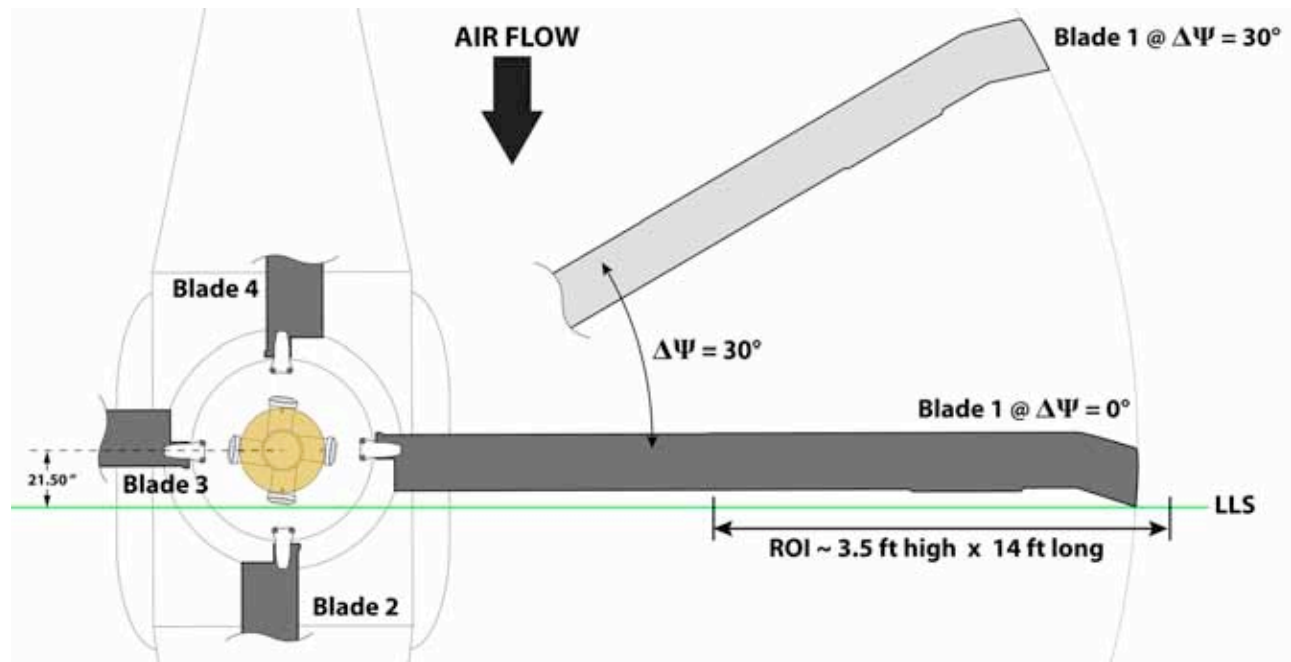


Figure 24. Measurement of PIV origin.

The laser trigger delay (measured from the IPR in encoder counts) required to achieve this condition was noted. A desired blade position ahead of the LLS, $\Delta\Psi$, was then established by simply increasing the laser trigger delay by a known amount from this reference value.

With the primary blade in the reference position ($\Delta\Psi = 0$) a small number of PIV images were acquired in order to define a local origin for the PIV measurements close to the blade tip. The tip trailing edge would appear as a hot spot in each image. These hot spot locations were used to define the PIV origin at each new rotor test condition. Twenty PIV frames were acquired to define the origin. A PIV frame consists of 4 images: a reference image and a delayed image from each of the two PIV cameras.

After the origin images were acquired, seed levels were adjusted by turning on one seeder for 2-3 minutes. All test section lights were turned off, except for an IR illuminator that was needed for a night-vision camera used to observe the rotor. The primary blade was positioned to the desired delayed azimuth. A single PIV frame was then acquired and evaluated. If the evaluation was acceptable, then 100 frames were acquired. The time between PIV data points was typically 10-12 minutes, which included 2-3 min to add seed, 2-3 min to evaluate a single frame, and 3-5 min to set up and acquire 100 frames. Rotor and tunnel condition data were acquired simultaneously with the PIV image data. For a given set of rotor conditions, PIV images were acquired for $\Delta\Psi = 0$ to 360 deg in varying increments of $\Delta\Psi$. During a run, the stream wise position of the laser sheet was checked and adjusted as required.

In general, populations of size 100 PIV frames were acquired for each blade position relative to the LLS, and simple ensemble averages for the velocity field computed. Populations were limited to either 100 or 200 PIV frames in order to maximize the number of blade positions documented at each rotor test condition. PIV wake data were measured behind each of the 4 rotor blades in order to document blade-to-blade differences.

Normally, PIV data would be acquired with a “hands off” protocol so that no rotor-operator induced perturbations were introduced into the measurements. In this particular wind tunnel test a trim controller was implemented at the Rotor Control Console that changed the blade pitch around the rotor revolution in such a manner as to minimize oscillations in rotor thrust and moments^{9,26}.

Simultaneous acquisition of both PIV and NFAC wind tunnel and rotor dependent test conditions was achieved by simple oral cue. No attempt was made to initiate data acquisition starting with a specific rotor revolution.

V. Results and Discussion

All PIV data presented in this report are referred to as *preliminary* in the sense that simple photogrammetric camera calibrations were used; no allowance has been made for motion of the LLS out of the calibration plane; simple ensemble averaging of velocity fields has been used, with no allowance for vortex wander; and the analysis grid is coarse (a constant window size of 32x32 pixels with 50% overlap was deemed adequate for identification of vortices). Final processing will require more advanced processing techniques --- auto-calibration to compensate for LLS motion, a high-resolution grid (to provide internal vortex structure), and conditional sampling (to compensate for vortex wander).

PIV data were acquired for the following conditions:

- 1) Simulated 1-g level flight, setting up on C_L , C_M and propulsive force (by change of shaft angle).
- 2) Matching Airloads flight test conditions by setting up on C_T/σ , moments from the mast-bending gage (not from the rotor balance) and corrected shaft angle (using wall effect corrections).
- 3) Parametric studies where shaft angle was set, then M_{tip} (by adjusting rotor RPM), then advance ratio (by adjusting test section velocity), then C_T or C_L (adjust T or L by changing collective pitch) and finally moments.

The original set of desired test conditions for PIV data acquisition included rotor stall conditions and conditions simulating previous flight test and small-scale wind tunnel test conditions. Prior to PIV data acquisition, airloads data were acquired at rotor stall conditions. During these highly unsteady flow conditions, the wind tunnel structure and control room experienced noticeable shaking. The decision was made to avoid such conditions to mitigate excessive vibration of the laser optics and PIV cameras. In addition, some rotor trim conditions caused the blade tip to rise up and out of the ROI. Certain hub rolling moment trim conditions were avoided since the blade tip was either below or above the ROI. Table 2 lists the test conditions where PIV data were acquired.

The RBOS measurements (acquired simultaneously with PIV data) are expected to provide information on the mean vortex filament orientation relative to the plane of the LLS, thereby allowing rotation of the PIV measurements into a plane orthogonal to the vortex filament.

Table 2. PIV Test Conditions

NFAC Run No.	Shaft Angle (deg)	M_{tip}	μ	C_T/σ	$\Delta\Psi$ (deg)
73	0	0.650	0.150	0.080	5, 15, 30, 45, 60, 75, 95, 135, 185, 225, 275, 315
75	4	0.650	0.150	0.080	5, 15, 30, 45, 60, 75, 95, 135, 185, 225, 275, 315
78	-4.82	0.638	0.303	0.087	5, 15, 30, 45, 60, 75, 95
81	0	0.650	0.240	0.070, 0.090	5
81	0	0.650	0.240	0.110	5, 15, 30, 45, 60, 75, 95, 185, 275
83	0	0.650	0.150	0.070, 0.090, 0.110, 0.120	15
83	-6.9	0.650	0.350	0.080	5, 10, 15, 20, 30, 45, 60, 75, 95, 185, 275

The test condition described in the current paper corresponds to an advance ratio of 0.150 with $C_T/\sigma = 0.080$ and the rotor shaft vertical. At this rotor test condition, the PIV flow field corresponding to the primary blade 30 degrees azimuth ahead of the LLS was selected for inclusion in the current paper.

Figure 25(a) presents the ensemble average velocity field (average of 100 instantaneous flow fields) for the complete PIV ROI. The maximum extent of the usable ROI is 1.16m (V) x 3.99m (H) (3.8ft x 13.1ft). The in-plane velocity components are drawn as vectors scaled with the free stream velocity (reference velocity, at same scale, is shown to the right of the legend in m/s). The out-of-plane velocity is presented as a contour plot. Four discrete zones were used to process the PIV images in order to maximize the available flow field coverage. Use of a relatively coarse 32x32 pixel cross-correlation window with 50% overlap resulted in a total of 20,828 vectors. Every second velocity vector in X and Y is skipped in Figure 25(a) for the purpose of clarity. Data are presented in a coordinate system with origin at the blade tip trailing edge as defined earlier.

Several features are immediately apparent. The velocity defect in the blade wake is clearly recognized as the horizontal band of blue near the bottom of the figure. Most noticeable about this trailed wake is the apparent dislocation of the wake in the center of the figure. This can be explained by the presence of a trim tab as shown in Figure 2. Most full-scale rotor blades are equipped with trim tabs. On a helicopter, the trim tabs are used to achieve blade tracking. In general, in rotor tests carried out in the NFAC, trim tabs are not changed from the “as delivered” state. Instead, blade tracking is normally achieved by adjusting individual pitch link rods to achieve acceptable track in hover (as used in the current test).

The vorticity field corresponding to this ensemble average velocity field is shown in Figure 25(b). Three rotor blade tip vortices are evident, and each is labeled to identify the blade of origin (see Figure 24 for blade numbering protocol). Positive vorticity is associated with CCW vortex rotation, and vice versa. Clearly, the peak vorticity associated with the tip vortex decreases rapidly with increasing wake age. Much weaker areas of vorticity can be identified in the blade wake, and discrete areas of vorticity have been identified and labeled with wake age to help understand the evolution of the flow field. The almost continuous horizontal strip of vorticity near the bottom of the figure represents the wake being shed by Blade 1 (located 30° ahead of the LLS) and extends all the way out to the blade tip. There is a horizontal strip of vorticity in the center of the figure with wake age $\psi_w = 120^\circ$ whose origin is the trim tab belonging to Blade 4, the blade 90° ahead of Blade 1 ($\psi_w = \Delta\Psi + 90^\circ = 120^\circ$). Figure 25(b) shows that the trim tab wake convects upwards and slightly inboard with increasing wake age, at least initially. Careful examination of the complete PIV dataset covering the full range of wake ages for this rotor test condition (see Table 2) reveals that the region of vorticity between the trim tab and the blade tip starts out horizontally oriented at

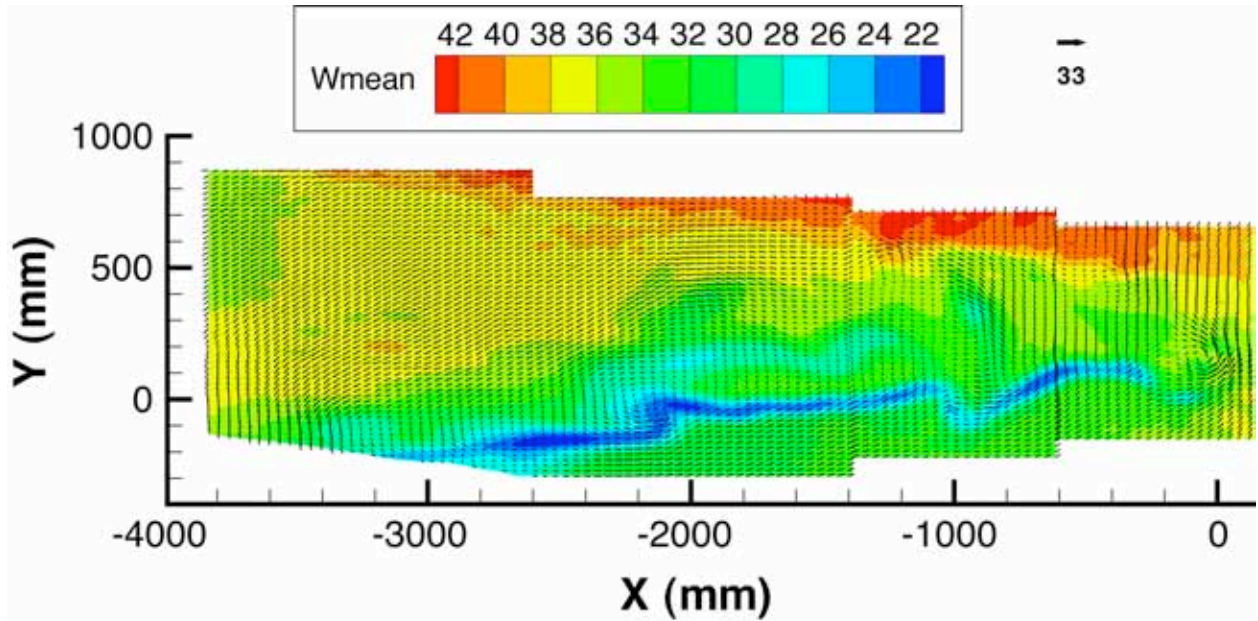


Figure 25(a). Contour plot of streamwise velocity W with scaled in-plane velocity vectors. (25% vectors shown)

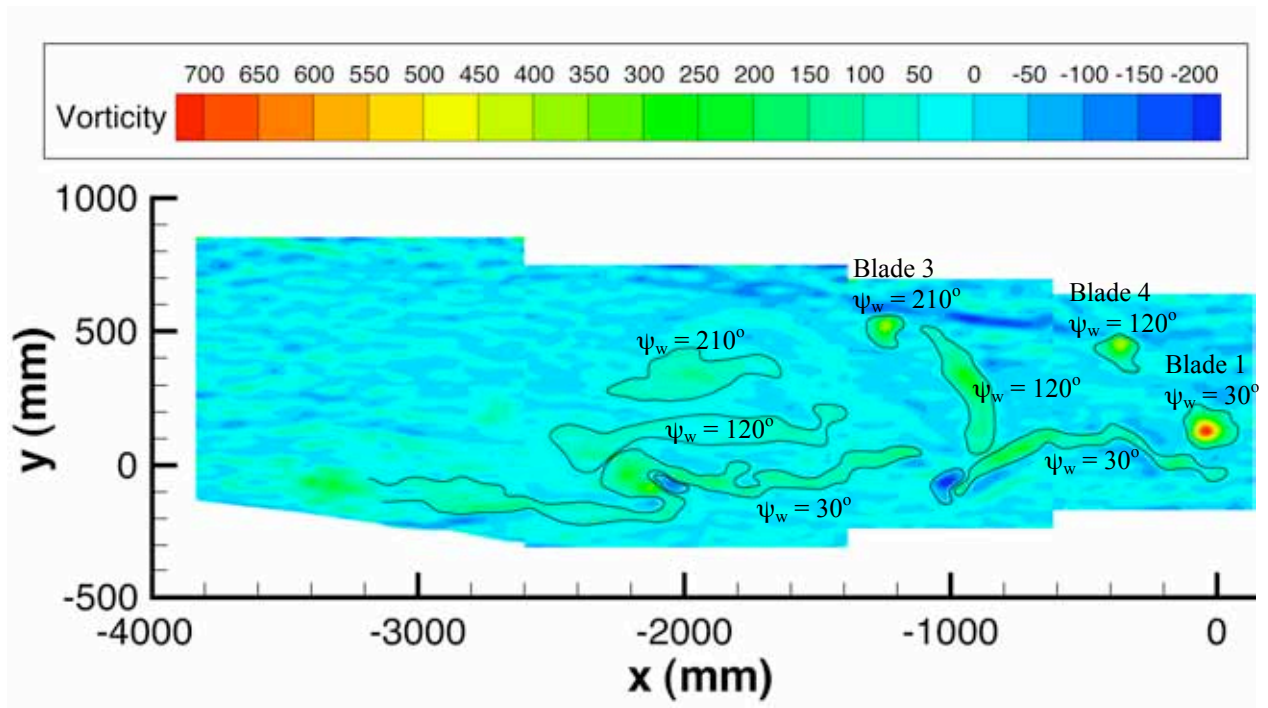


Figure 25(b). Contour plot of streamwise vorticity.

$\psi_w = 30^\circ$ but rotates to the vertical position shown for $\psi_w = 120^\circ$ and then continues rotating to the horizontal position labeled $\psi_w = 210^\circ$. All concentrations of vorticity labeled $\psi_w = 30^\circ$ in Figure 25(b) have Blade 1 as origin, $\psi_w = 120^\circ$ have Blade 4 as origin, and $\psi_w = 210^\circ$ have Blade 3 as origin.

Figure 26 shows a close up of the trim tab velocity field. One hundred per cent of the vectors are shown. The CCW rotation of the vortex at the inboard end of the trim tab and the CW rotation of the vortex at the outboard end of the trim tab are consistent with the upward displacement of the trim tab wake. Since trim tab deflections are not normally included in computational efforts to model the UH-60 rotor flow, the trim tab deflection for each of the 4 blades was documented at the end of the test (both before and after removal from the model to protect against changes occurring during the removal process). All 4 blades were found to have very similar physical trim tab settings. All trim tabs were determined to be deflected upwards, consistent with the observed displacement of the trim tab wake. Careful examination of Figure 26 reveals the velocity defect associated with the trim tab for both $\psi_w = 30^\circ$ and $\psi_w = 120^\circ$.

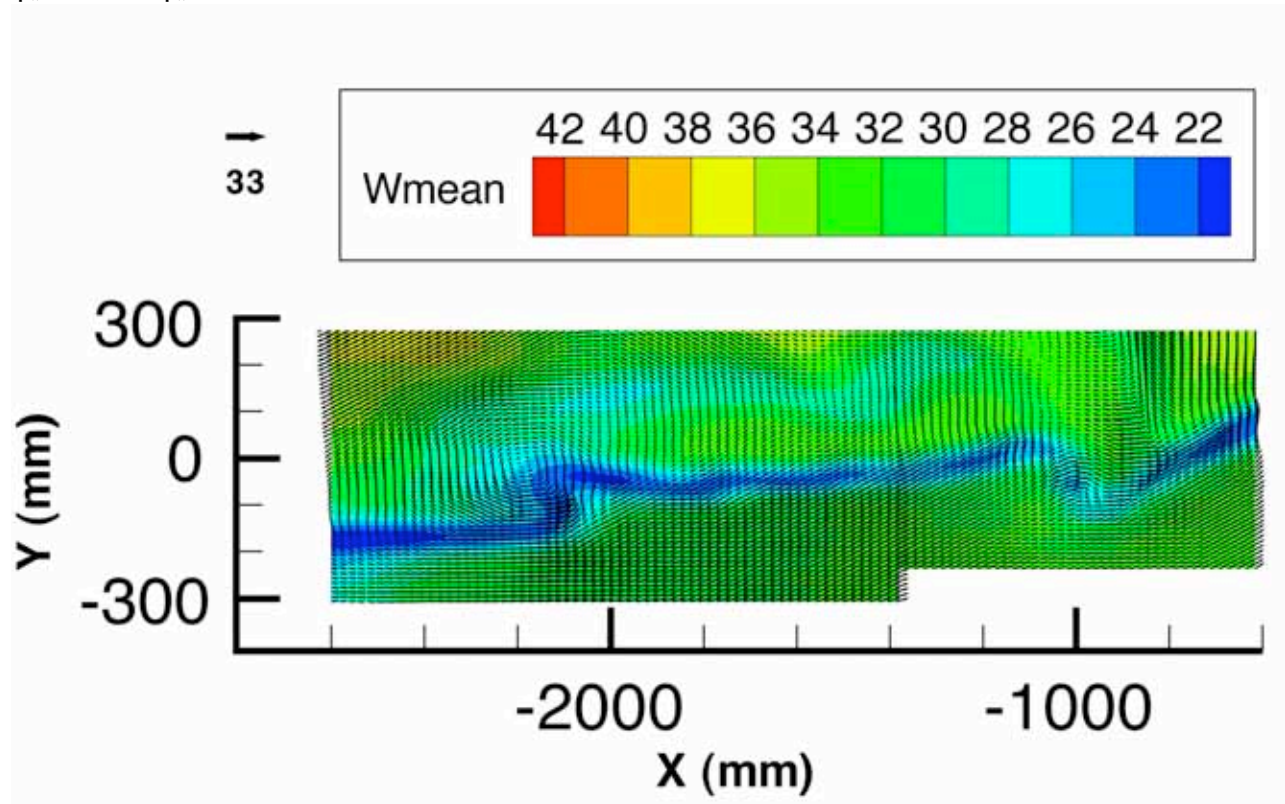


Figure 26. Velocity field in the wake of the trim tab.

Figure 27(a) shows a close up of the outer 1/3 of the PIV flow field with 100% of the in-plane vectors displayed. This figure is more than adequate to reveal the presence of three rotor blade tip vortices and indicates the richness of the data even with the coarse grid chosen for preliminary analysis. Figure 27(b) shows the corresponding vorticity field. Unlike Figure 25(b), Figure 27(b) uses an identical range for both positive and negative vorticity, revealing that the most important concentrations of stream wise vorticity lie within the tip vortices. The vorticity in the trailed vortex sheets is considerably weaker. The upward trajectory of the tip vortices for $0 < \psi_w < 210^\circ$ came as a surprise to some observers, since the rotor wake must eventually move downwards, opposite to the direction of rotor thrust.

Figure 28 shows a close up view of the streamwise vorticity associated with the tip vortex at wake age $\psi_w = 30^\circ$ (Blade 1). Scaled in-plane velocity vectors are shown (100% of available vectors) and the reference (free-stream)

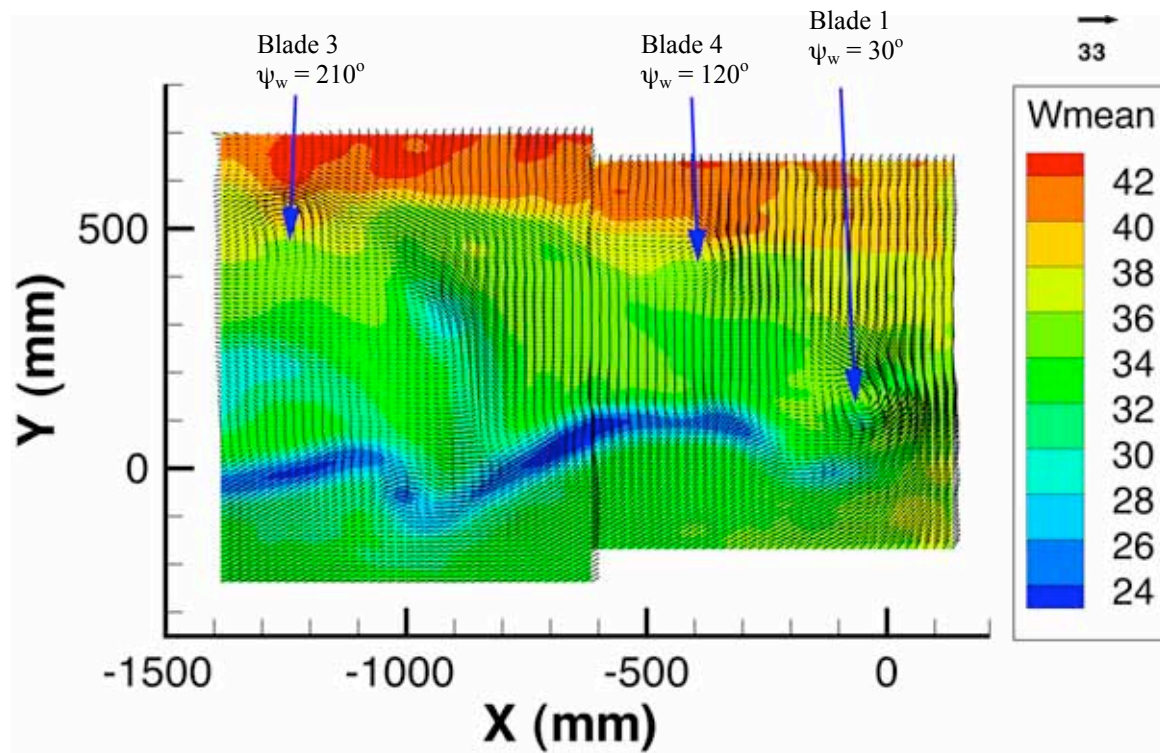


Figure 27(a). Velocity field near the blade tip
(100% vectors shown)

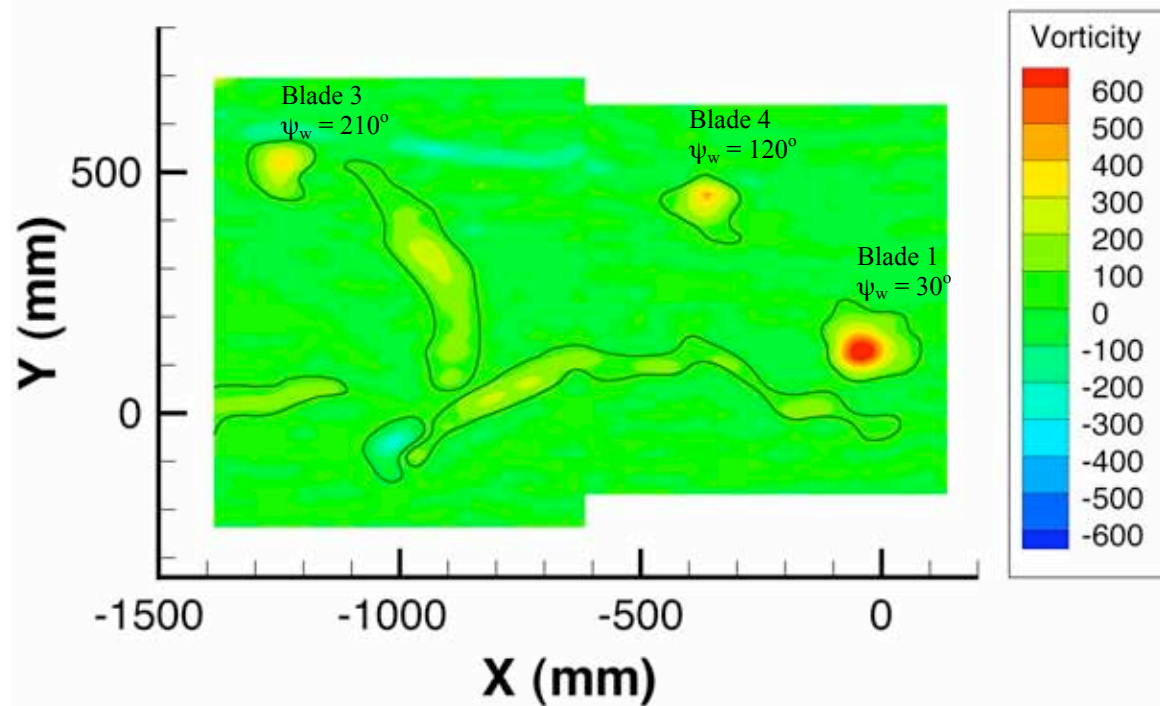


Figure 27(b). Vorticity field near the blade tip.

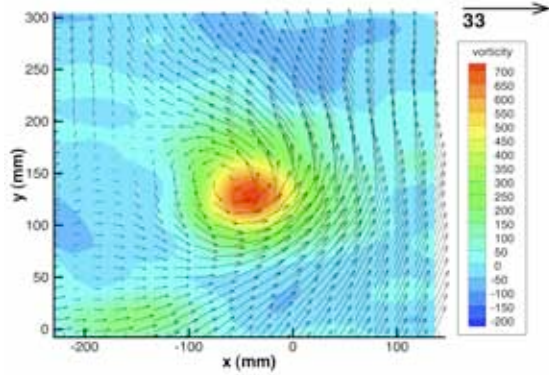


Figure 28. Vorticity distribution and scaled in-plane velocities associated with tip vortex, $\psi_w = 30^\circ$.

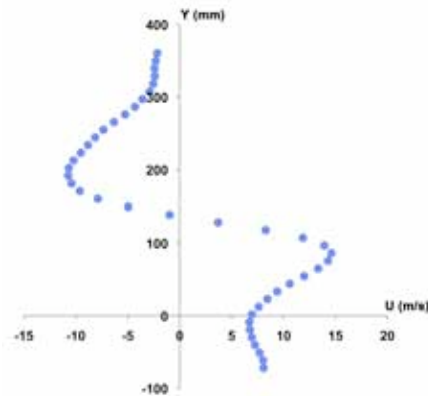


Figure 29. Velocity distribution, $U(y)$ through tip vortex.

velocity vector (in m/s) included for comparison. Note that the vectors inside the vortex core indicate that the vortex is moving to the right (positive u) and upwards (positive v).

By inspection, a vertical cut was made through the vortex center and the variation of horizontal velocity along this line is shown in Figure 29. The velocity distribution differs from that expected from a stationary axisymmetric vortex because this vortex is not stationary (as pointed out above). Note that a significant velocity gradient also exists across the vortex. No (meaningful) statement can be made regarding vortex core diameter or vortex structure as the current preliminary data are derived from a simple ensemble average velocity field and therefore suffer from vortex wander.

The next step is to re-process the PIV data with a high-resolution grid in the neighborhood of each vortex using the current data to identify each region to be re-processed. Conditional averaging will then be used to compensate for vortex wander. This is normally accomplished by identifying the instantaneous vortex center location using the centroid of vorticity (or an alternative metric) and aligning the vortices before evaluating the average velocity field. Only then will meaningful vortex parameters such as core diameter and vortex structure be available for comparison with model-scale hover data^{16,17} and full-scale forward flight measurements²⁷.

One disadvantage of this approach is that it employs vorticity to identify the instantaneous vortex center. Instantaneous velocity fields are often quite noisy in themselves and instantaneous vorticity fields are even noisier. Other metrics used to identify the vortex center also involve differentiating the instantaneous velocity field and therefore suffer the same problem as vorticity. However, by curve-fitting the instantaneous *velocity* field of each vortex to that of a model vortex (Lamb vortex, for example) in order to determine the instantaneous vortex parameters, vortex wander effects can be eliminated by averaging over the population for each vortex parameter. This approach²⁸ has several attractive features in that the instantaneous velocity fields are used to determine the vortex parameters instead of the vorticity fields, maximum and minimum values can be provided for vortex strength and tangential velocity (for example), and confidence estimates can be provided for each vortex parameter.

VI. Conclusions

Some of the difficulties encountered in applying Particle Image Velocimetry to testing in the National Full-Scale Aerodynamic Complex (NFAC) 40-Ft x 80-Ft Wind Tunnel have been described. Forward-flight testing of a full-scale UH-60A rotor system of diameter 53.66ft was discussed in detail. Preliminary PIV data were presented in terms of simple ensemble averages of velocity and vorticity. Such averages include the effects of vortex wander and prohibit any meaningful statements regarding vortex core diameter or vortex structure. It is planned to re-process the PIV data in the neighborhood of each vortex using a high-resolution grid and more sophisticated commercial software. Conditional averaging will be used to minimize the effects of vortex wander.

Only the smallest glimpse into the available PIV data has been provided, but the apparent richness of the data has been illustrated. Very little full-scale rotor wake data are currently available for correlation with CFD computations. The current dataset hopes to eliminate this deficiency.

Acknowledgments

The authors wish to thank the UH-60A Airloads test crew of the National Full-Scale Aerodynamics Complex for enabling the PIV measurements. Particular thanks are extended to Charles Rogers and Jose Navarrete of Jacobs Engineering. We also greatly appreciate the contributions of Louise Walker (Aerospace Computing, Inc.); Dr. Manikandan Ramasamy (UARC, NASA Ames); and Luther Jenkins, Dr. C. S. Yao, and Scott Bartram (NASA Langley). The efforts of James T. Heineck of NASA Ames are also recognized. His many helpful suggestions and his work in tailoring the laser sheet optics contributed greatly to the successful acquisition of the PIV measurements. Finally, Dr. Wayne Johnson is recognized for performing CAMRAD II calculations that helped us optimize the position of the LLS.

This work was sponsored by the Subsonic Rotary Wing Project of the NASA Fundamental Aeronautics Program.

References

- ¹Holst, T. L. and Pulliam, T. H., "Optimization of Overset Solution Adaptive Grids for Hovering Rotorcraft Flows," *American Helicopter Society Aeromechanics Specialists' Conference*, San Francisco, CA, January 2010.
- ²Nielsen, E. J., Lee-Rausch, E. M. and Jones, W. T., "Adjoint-Based Design of Rotors Using the Navier-Stokes Equations in a Non-inertial Reference Frame," *American Helicopter Society 65th Annual Forum*, Grapevine, TX, May 2009.
- ³Yamauchi, G. K. and Young, L. A., Editors, "A Status of NASA Rotorcraft Research," NASA/TP-2009-215369, September 2009.
- ⁴Jenkins, L. N., Yao, C.-S., Bartram, S. M., Harris, J., Allan, B. G., Wong, O. D. and Mace, W. D., "Development of a Large Field-of-View PIV System for Rotorcraft Testing in the 14- x 22-Foot Subsonic Wind Tunnel," *American Helicopter Society 65th Annual Forum*, Grapevine, TX, May 2009.
- ⁵Allan, B. G., Jenkins, L. N., Yao, C.-S., Bartram, S. M., Hallissy, J. B., Harris, J., Noonan, K. W., Wong, O. D., Jones, H. E., Malovrh, B. D., Reis, D. G. and Mace, W. D., "Navier-Stokes Simulation of a Heavy Lift Slowed-Rotor Compound Helicopter Configuration," *American Helicopter Society 65th Annual Forum*, Grapevine, TX, May 2009.
- ⁶Heineck, J. T., Kushner, L. K., Schairer, E. T. and Walker, L. A., "Retro-reflective Background Oriented Schlieren (RBOS) as applied to Full-Scale UH-60 Blade Tip Vortices," *American Helicopter Society Aeromechanics Specialists' Conference*, San Francisco, CA, January 2010.
- ⁷Olson, L. E., Abrego, A. I., Barrows, D. A. and Burner, A. W., "Blade Deflection Measurements of a Full-Scale UH-60A Rotor System," *American Helicopter Society Aeromechanics Specialists' Conference*, San Francisco, CA, January 2010.
- ⁸Wong, O. D., Noonan, K. W., Watkins, A. N., Jenkins, L. N. and Yao, C.-S., "Non-Intrusive Measurements of a Four-Bladed Rotor in Hover – A First Look," *American Helicopter Society Aeromechanics Specialists' Conference*, San Francisco, CA, January 2010.
- ⁹Norman, T. R., Theodore, C., Shinoda, P. M., Fuerst, D., Arnold, U. T. P., Makinen, S., Lorber, P. and O'Neill, J., "Full-Scale Wind Tunnel Test of a UH-60 Individual Blade control System for Performance Improvement and Vibration, Loads, and Noise Control," *American Helicopter Society 65th Annual Forum*, Grapevine, TX, May 2009.
- ¹⁰Norman, T. R., Shinoda, P. M., Peterson, R. L. and Datta, A., "Full-Scale Wind Tunnel Test of the UH-60A Airloads Rotor," *American Helicopter Society 67th Annual Forum*, Virginia Beach, VA, May 2011.
- ¹¹Kufeld, R. M., Balough, D. L., Cross, J. L., Studebaker, K. F., Jennison, C. D. and Bousman, W. G., "Flight Testing the UH-60A Airloads Aircraft," *American Helicopter Society 50th Annual Forum*, Washington, D. C., May 1994.
- ¹²Norman, T. R., Shinoda, P. M., Kitaplioglu, C., Jacklin, S. A. and Shekman, A., "Low-Speed Wind Tunnel Investigation of a Full-Scale UH-60 Rotor System," *American Helicopter Society 58th Annual Forum*, Montreal, Canada, June 2002.
- ¹³Yeo, H., Bousman, W. and Johnson, W., "Performance Analysis of a Utility Helicopter with Standard and Advanced Rotors," *American Helicopter Society Aerodynamics, Acoustics and Test and Evaluation Meeting*, San Francisco, CA, January 2002.
- ¹⁴Coleman, C. P. and Bousman, W. G., "Aerodynamic Limitations of the UH-60A Rotor," *American Helicopter Society Aeromechanics Specialists Conference*, San Francisco, CA, January 1994.
- ¹⁵Heineck, J. T., Yamauchi, G. K., Wadcock, A. J., Lourenco, L. and Abrego, A. I., "Application of Three-Component PIV to a Hovering Rotor Wake," *American Helicopter Society 56th Annual Forum*, Virginia Beach VA, May 2-4, 2000.
- ¹⁶Leishman, J. G. and Bagai, A., "Challenges in Understanding the Vortex Dynamics of Helicopter Rotor Wakes," *AIAA Journal*, Vol. 36, No. 7, July 1998.
- ¹⁷Bhagwat, M. J. and Leishman, J. G., "Correlation of Helicopter Rotor Tip Vortex Measurements," *AIAA Journal*, Vol. 38, No. 2, February 2000.

¹⁸Yamauchi, G. K., Johnson, W. and Wadcock, A. J., "Vortex Wake Geometry of a Model Tilt-Rotor in Forward Flight," Heli Japan 2002, *AHS International Meeting on Advanced Rotorcraft Technology and Life Saving Activities*, Tochigi, Japan, November 11-13, 2002.

¹⁹Johnson, W., Yamauchi, G. K., Derby, M. R. and Wadcock, A. J., "Wind Tunnel Measurements and Calculations of Aerodynamic Interactions Between Tilt-Rotor Aircraft," *41st Aerospace Sciences Meeting and Exhibit*, Reno, Nevada, January 6-9, 2003.

²⁰Yamauchi, G. K., Wadcock, A. J. and Derby, M. R., "Measurement of the Aerodynamic Interaction of Two Tilt-Rotors," *American Helicopter Society 59th Annual Forum*, Phoenix, Arizona, May 6-8, 2003.

²¹Wadcock, A. J., Yamauchi, G. K., Heineck, J. T., Silva, M. J. and Long, K. R., "PIV Measurements of the Wake of a Tandem-Rotor Helicopter in Proximity to a Ship," *American Helicopter Society 4th Decennial Specialists' Conference on Aeromechanics*, San Francisco, CA, January 12-13, 2004.

²²Silva, M. J., Yamauchi, G. K., Wadcock, A. J. and Long, K. R., "Wind Tunnel Investigation of the Aerodynamic Interactions Between Helicopters and Tilt-Rotors in a Shipboard Environment," *American Helicopter Society 4th Decennial Specialists' Conference on Aeromechanics*, San Francisco, CA, January 12-13, 2004.

²³Rajagopalan, R. G., Schaller, D. F., Wadcock, A. J., Yamauchi, G. K., Heineck, J. T. and Silva, M. J., "Experimental and Computational Simulation of a Model Ship in a Wind Tunnel," *43rd AIAA Aerospace Sciences Meeting*, Reno, NV, January 10-13, 2005.

²⁴Silva, M. J., Wadcock, A. J., Yamauchi, G. K., van Aken, J. M. and Shinoda, P. M., "Wind Tunnel Investigation of the Shipboard Aerodynamic Interactions Inducing the V-22 Tilt-Rotor Un-commanded Roll-On-Deck Response," *American Helicopter Society 61st Annual Forum*, Grapevine, TX, June 1-3, 2005.

²⁵Romander, E. A., Betzina, M. D., Silva, M. J., Wadcock, A. J. and Yamauchi, G. K., "Investigating Tilt-Rotor Formation Flight via 1/48th-Scale Wind Tunnel Experiment," *American Helicopter Society 62nd Annual Forum*, Phoenix, AZ, May 9-11, 2006.

²⁶Theodore, C. R. and Tischler, M. B., "Development and Operation of an Automatic Rotor Trim Control System for the UH-60 Individual Blade Control Wind Tunnel Test," *American Helicopter Society Specialists' Conference on Aeromechanics*, San Francisco, CA, January 20-22, 2010.

²⁷McKenzie, R. L. and Reinath, M. S., "Three-Dimensional Planar Doppler Velocity Measurements in a Full-Scale Rotor Wake," *AIAA Journal*, Vol. 43, No. 3, March 2005.

²⁸Ramasamy, M., Paetzel, R. and Bhagwat, M. J., "Aperiodicity Correction for Rotor Tip Vortex Measurements", *AHS 67th Annual Forum*, Virginia Beach, VA, May 3-5, 2011.